Effects of sample arm motion in endoscopic polarization-sensitive optical coherence tomography

Mark C. Pierce, Milen Shishkov, B. Hyle Park, Nader A. Nassif, Brett E. Bouma, Guillermo J. Tearney, Johannes F. de Boer

Wellman Center for Photomedicine, Harvard Medical School
Massachusetts General Hospital BAR 714, Boston, MA 02114
pierce@helix.mgh.harvard.edu
deboer@helix.mgh.harvard.edu

Abstract: Motion of the sample arm fiber in optical coherence tomography (OCT) systems can dynamically alter the polarization state of light incident on tissue during imaging, with consequences for both conventional and polarization-sensitive (PS-)OCT. Endoscopic OCT is particularly susceptible to polarization-related effects, since in most cases, the transverse scanning mechanism involves motion of the sample arm optical fiber to create an image. We investigated the effects of a scanning sample arm fiber on the polarization state of light in an OCT system, and demonstrate that by referencing the state backscattered from within a sample to the measured state at the surface, changes in polarization state due to sample fiber motion can be isolated. The technique is demonstrated by high-speed PS-OCT imaging at 1 frame per second, with both linear and rotary scanning fiber-optic probes. Measurements were made on a calibrated wave plate, and endoscopic PS-OCT images of *ex-vivo* human tissues are also presented, allowing comparison with features in histologic sections.

OCIS codes: (170.4500) Optical coherence tomography; (170.2150) Endoscopic imaging; (230.5440) Polarization-sensitive devices

References and links

1. B. E. Bouma, G. J. Tearney, "Clinical imaging with optical coherence tomography," Acad. Radiol. **9**, 942-953 (2002).
2. F. I. Feldchtein, G. V. Gelikonov, V. M. Gelikonov, R. V. Kuranov, A. M. Sergeev, N. D. Gladkova, A. V. Shakhov, N. M. Shakhova, L. B. Snopova, A. B. Terent'eva, E. V. Zagainova, Y. P. Chumakov, I. A. Kuznetzova, "Endoscopic applications of optical coherence tomography," Opt. Express **3**, 257-270 (1998).
3. G. J. Tearney, S. A. Boppart, B. E. Bouma, M. E. Brezinski, N. J. Weissman, J. F. Southern, J. G. Fujimoto, "Scanning single-mode fiber optic catheter-endoscope for optical coherence tomography," Opt. Lett. **21**, 543-545 (1996).
4. G. J. Tearney, M. E. Brezinski, B. E. Bouma, S. A. Boppart, C. Pitris, J. F. Southern, J. G. Fujimoto, "*In vivo* endoscopic optical biopsy with optical coherence tomography," Science **276**, 2037-2039 (1997).
5. B. E. Bouma, G. J. Tearney, "Power-efficient nonreciprocal interferometer and linear-scanning fiber-optic catheter for optical coherence tomography," Opt. Lett. **24**, 531-533 (1999).
6. A. M. Rollins, R. Ung-arunyawee, A. Chak, R. C. K. Wong, K. Kobayashi, M. V. Sivak, Jr., J. A. Izatt, "Real-time *in vivo* imaging of human gastrointestinal ultrastructure by use of endoscopic optical coherence tomography with a novel efficient interferometer design," Opt. Lett. **24**, 1358-1360 (1999).
7. P. R. Herz, Y. Chen, A. D. Aguirre, J. G. Fujimoto, H. Mashimo, J. Schmitt, A. Koski, J. Goodnow, C. Petersen, "Ultrahigh resolution optical biopsy with endoscopic optical coherence tomography," Opt. Express **12**, 3252-3542 (2004).
8. Y. Pan, H. Xie, G. K. Fedder, "Endoscopic optical coherence tomography based on a microelectromechanical mirror, Opt. Lett. **26**, 1966-1968 (2001).
9. P. H. Tran, D. S. Mukai, M. Brenner, Z. Chen, "*In vivo* endoscopic optical coherence tomography by use of a rotational microelectromechanical system probe," Opt. Lett. **29**, 1236-1238 (2004).

#7740 - $15.00 US Received 7 June 2005; revised 13 July 2005; accepted 14 July 2005

10. P. R. Herz, Y. Chen, A. D. Aguirre, K. Schneider, P. Hsiung, J. G. Fujimoto, K. Madden, J. Schmitt, J. Goodnow, C. Petersen, "Micromotor endoscope catheter for *in vivo*, ultrahigh-resolution optical coherence tomography," Opt. Lett. **29**, 2261-2263 (2004).
11. J. F. de Boer, T. E. Milner, M. J. C. van Gemert, J. S. Nelson, "Two-dimensional birefringence imaging in biological tissue by polarization-sensitive optical coherence tomography," Opt. Lett. **22**, 934-936 (1997).
12. M. J. Everett, K. Schoenenberger, B. W. Colston, Jr., L. B. Da Silva, "Birefringence characterization of biological tissue by use of optical coherence tomography," Opt. Lett. **23**, 228-230 (1998).
13. J. F. de Boer, T. E. Milner, J. S. Nelson, "Determination of the depth-resolved Stokes parameters of light backscattered from turbid media by use of polarization-sensitive optical coherence tomography," Opt. Lett. **24**, 300-302 (1999).
14. G. Yao, L. V. Wang, "Two-dimensional depth-resolved Mueller matrix characterization of biological tissue by optical coherence tomography," Opt. Lett. **24**, 537-539 (1999).
15. C. K. Hitzenberger, E. Götzinger, M. Sticker, M. Pircher, A. F. Fercher, "Measurement and imaging of birefringence and optic axis orientation by phase resolved polarization sensitive optical coherence tomography," Opt. Express **9**, 780-790 (2001).
16. J. Moreau, V. Loriette, A-C. Boccara, "Full-field birefringence imaging by thermal-light polarization-sensitive optical coherence tomography. II. Instrument and results," Appl. Opt. **42**, 3811-3818 (2003).
17. N. J. Kemp, J. Park, H. N. Zaatari, H. G. Rylander, T. E. Milner, "High-sensitivity determination of birefringence in turbid media with enhanced polarization-sensitive optical coherence tomography," J. Opt. Soc. Am. A **22**, 552-560 (2005).
18. C. E. Saxer, J. F. de Boer, B. H. Park, Y. Zhao, Z. Chen, J. S. Nelson, "High-speed fiber-based polarization-sensitive optical coherence tomography of *in vivo* human skin," Opt. Lett. **25**, 1355-1357 (2000).
19. J. E. Roth, J. A. Kozak, S. Yazdanfar, A. M. Rollins, J. A. Izatt, "Simplified method for polarization-sensitive optical coherence tomography," Opt. Lett. **26**, 1069-1071 (2001).
20. M. C. Pierce, B. H. Park, B. Cense, J. F. de Boer, "Simultaneous intensity, birefringence, and flow measurements with high-speed fiber-based optical coherence tomography," Opt. Lett. **27**, 1534-1536 (2002).
21. S. L. Jiao, W. R. Yu, G. Stoica, L. H. V. Wang, "Optical-fiber-based Mueller optical coherence tomography," Opt. Lett. **28**, 1206-1208 (2003).
22. D. P. Davé, T. Akkin, T. E. Milner, "Polarization-maintaining fiber-based optical low-coherence reflectometer for characterization and ranging of birefringence," Opt. Lett. **28**, 1775-1777 (2003).
23. S. Guo, J. Zhang, L. Wang, J. S. Nelson, Z. Chen, "Depth-resolved birefringence and differential optical axis orientation measurements with fiber-based polarization-sensitive optical coherence tomography," Opt. Lett. **29**, 2025-2027 (2004).
24. B. H. Park, M. C. Pierce, B. Cense, J. F. de Boer, "Real-time multi-functional optical coherence tomography,"Opt. Express **11**, 782-793 (2003).
25. B. H. Park, M. C. Pierce, B. Cense, S-H Yun, M. Mujat, G. J. Tearney, B. E. Bouma, J. F. de Boer, "Real-time fiber-based multi-functional spectral-domain optical coherence tomography at 1.3 μm,"Opt. Express **13**, 3931-3944 (2005).
26. P. R. Wheater, H. G. Burkitt, V. G. Daniels, *Functional Histology*, 2nd Ed., Ch. 8 (Churchill Livingstone, New York, 1987).
27. J. Strasswimmer, M. C. Pierce, B. H. Park, V. Neel, J. F. de Boer, "Polarization-sensitive optical coherence tomography of invasive basal cell carcinoma," J. Biomed. Opt. **9**, 292-298 (2004).
28. M. C. Pierce, J. Strasswimmer, B. H. Park, B. Cense, J. F. de Boer, "Advances in optical coherence tomography for dermatology," J. Invest. Dermatol. **123**, 458-463 (2004).
29. B. Cense, T. C. Chen, B. H. Park, M. C. Pierce, J. F. de Boer, "Thickness and birefringence of healthy retinal nerve fiber layer tissue measured with polarization-sensitive optical coherence tomography," Invest. Ophthalmol. Vis. Sci. **45**, 2606-2612 (2004).

1. Introduction

Fiber-optic probes compatible with medical endoscopes and catheters have enabled optical coherence tomography (OCT) imaging of previously inaccessible regions within the human body [1,2]. The high-resolution imaging capability of OCT has been demonstrated in many applications related to internal organs and structures, and when coupled with high-speed interferometer systems and real-time image display, endoscopic OCT can provide a unique diagnostic tool for the clinic.

Several different probe designs and scanning configurations have been reported, each tailored to a particular medical specialty. Standard single-mode optical fiber delivers light to the site of interest, with micro-optical components used to focus and direct the optical beam at the distal end of the probe. In many probe devices, these fibers and optics are incorporated

#7740 - $15.00 US Received 7 June 2005; revised 13 July 2005; accepted 14 July 2005

within and affixed to a wound cable, capable of transducing proximal motion from outside the body to distal motion at the catheter or endoscope tip. Proximal linear or circumferential scanning of the wound cable and associated optics produces a similar motion of the focused beam at the sample, thereby enabling formation of the OCT image [3-7]. For applications in cardiology, probes of around 1 mm diameter can be scanned with an optical rotary junction, producing a radial image display, similar in format to intravascular ultrasound systems. In larger-lumen channels such as the gastrointestinal tract, circumferential scanning may result in distant surfaces appearing out of focus due to the limited depth of focus of the probe. For such situations, linear scanning devices were developed [5], producing OCT images in the familiar transverse geometry. While a few investigators have developed probes that incorporate miniature scanning mechanisms at the distal tip [8-10], transduction of proximal motion to the distal optics by means of a wound cable remains the most convenient method for transverse scanning in endoscopic and catheter-based OCT, especially when the probe diameter is constrained.

Recent extensions to conventional OCT imaging include polarization-sensitive (PS)-OCT, which may provide additional information on tissue functionality by determining the polarizing properties of a sample. Free-space PS-OCT systems [11-17] constructed using bulk optical components allow the polarization state of light to be controlled at each location in the interferometer. Traditionally, this has enabled uniform samples to be probed with a single circularly polarized incident state, ensuring detection of birefringence regardless of the sample's optic axis orientation. Multiple incident states can also be used to reduce the effects of speckle noise through averaging, and ensure reliable measurement in samples comprising multiple birefringent layers, including the eye [17].

Development of fiber-based PS-OCT [18-25] has relaxed issues associated with system handling and alignment, enabling construction of robust devices for clinical use. However, due to the random birefringence of conventional single-mode fiber, explicit knowledge of the polarization state of light in the system is lost, and certain fixed parameters in the bulk system, including circularity of incident light, cannot be guaranteed. In such circumstances, multiple incident polarization states and generalized analysis algorithms are required in order to correctly determine the polarizing properties of a sample. PS-OCT systems have also been constructed using polarization-maintaining (PM) fiber [22], where a linear polarization state launched along the fast or slow fiber axis is maintained on propagation to the sample. In this case, either multiple input states are again required, or a single linear input state can be used with a quarter wave plate immediately prior to the sample [22], to provide circularly polarized incident light. Due to the intrinsic birefringence of PM fiber, phase information is lost unless the sample arm comprises precisely-matched, orthogonally-spliced fiber sections, to ensure that light in orthogonal polarization channels travels equal optical path lengths [22]. As with conventional single-mode fiber-based PS-OCT, PM fiber systems remain susceptible to additional dynamic birefringence induced by fiber motion and bending.

Incorporation of a scanning fiber probe in the sample arm presents additional difficulties, as the entire sample arm fiber is in motion during acquisition of an image. This motion dynamically changes the fiber birefringence, producing a continuous variation in the polarization state of light incident on the sample during image acquisition. PS-OCT data processing algorithms assuming a known or constant incident polarization state are likely to produce erroneous results if applied to fiber-based systems with significant sample arm motion during imaging. Changes in polarization induced by scanning motion in fiber probes may also lead to image artifacts in conventional OCT systems operating without polarization diversity detection.

We investigated the effects of using linear and rotary scanning fiber-optic probes in a fiber-based PS-OCT system. Motion of the sample arm fiber is shown to change the polarization state of incident light during imaging, and is quantified in terms of the evolution of Stokes vectors on the Poincaré sphere. Previous fiber-based PS-OCT systems held the sample arm stationary or incurred only minimal amounts of bending during image acquisition, performing transverse scanning externally in free-space at the distal end of the fiber. In such

#7740 - $15.00 US Received 7 June 2005; revised 13 July 2005; accepted 14 July 2005

circumstances, the incident polarization state can be assumed to remain constant during acquisition of an image, and an average state at the sample surface can be determined from all or some range of A-lines within an image [18, 20, 24]. Birefringence in the sample arm fiber can then be isolated by making a relative measurement between the average surface polarization state, and each state backscattered from within the sample for each A-line. We show here that when the incident state changes during imaging, fiber-based endoscopic PS-OCT imaging can still be performed. This is achieved by quantifying the variation in surface Stokes vectors between A-lines, again sampling the surface state for each A-line, and averaging Stokes parameters over the range of neighboring A-lines for which polarization changes remain small.

2. Methods

Two fiber-optic probes were incorporated with an existing PS-OCT system [20], which uses a semiconductor-based optical source centered at 1320 nm, resulting in a measured coherence length of 14.7 μm in air. This time-domain system acquires and displays images at a rate of 1 frame per second. The first fiber probe was a linear scanning device [5], consisting of a length of conventional single-mode optical fiber (Corning SMF-28) inside a wound, multilayer cable. The proximal end of the cable is translated by a linear motor to convey motion to the distal optics, containing a gradient index lens to focus the beam, which exits the probe in a direction perpendicular to the fiber axis. The entire probe was enclosed in a stationary transparent sheath, resulting in an overall outer diameter of 2.0 mm (6 F). The acquisition speed was 2000 A-lines per second, with a 1.2 mm axial scan range (n = 1.4).

The second probe used the same micro-optic components to focus and direct the beam perpendicular to the fiber axis, but in this case, performed circumferential scanning by means of an optical rotary junction at the proximal end [4]. Designed for intravascular use, this probe has an outer diameter of 1.0 mm (3 F), and was used with an acquisition speed of 1000 A-lines per second and a 1.5 mm axial scan range (n = 1.4). Both fiber-optic probes comprised moving fiber sections 1.4 m in length, and were extended (but not fixed) in a straight position for imaging.

3. Results

3.1 Incident polarization states

In a fiber-based OCT system, the polarization state of light is generally unknown, and consequently, the polarizing properties of a sample cannot be correctly determined under all circumstances with only a single, unknown incident state. To ensure that birefringence never goes undetected, we modulate the polarization state of light from the broadband source between two different states, orthogonal in the Poincaré sphere (e.g., linear horizontal and linear at 45°), for alternate A-lines [18, 20]. Figure 1 shows the endpoints of the calculated Stokes vectors describing these two polarization states of light at the detectors, as a single image is acquired. This signal was obtained from the small amount of light reflected from the surface of the gradient index lens or prism at the distal end of each probe, and therefore represents the polarization state on double-pass through the system. On the left, with the linear scanning probe held stationary, the Stokes vectors representing the two polarization states (colored green and blue) remain almost unchanged. In contrast, when the linear probe is scanned over a distance of 4 mm (center), the polarization states of light detected from the distal tip change during the 1 second required to generate a single image. This is indicated by an evolution of both Stokes vectors from their initial states, over the surface of the Poincaré sphere. In the right hand sphere, the polarization states of light detected from the tip of the rotary probe change more rapidly, as the probe undergoes a full 360º scan.

#7740 - $15.00 US Received 7 June 2005; revised 13 July 2005; accepted 14 July 2005

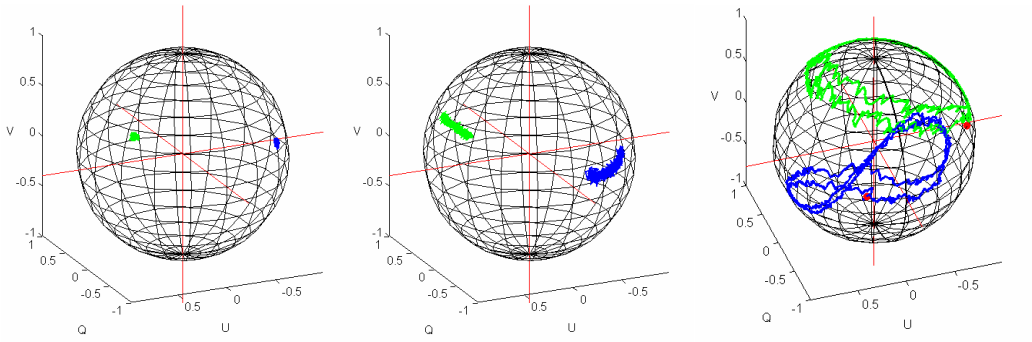

Fig. 1. Evolution of the polarization states of light detected from the distal end of each fiber probe during image acquisition, for a stationary probe (left), linear scanning probe (center), and rotary scanning probe (right). Polarization states are displayed on the Poincaré sphere as endpoints of the calculated Stokes vectors at the detectors, on double-pass following reflection at the distal tip.

Without motion of the sample arm fiber during imaging (Fig. 1, left), no time-dependent birefringence is induced, and in principle, the polarization states of light incident on the sample will remain constant. In practice, some spread in location of the Stokes vectors on the surface of the Poincaré sphere will arise due to the presence of noise in determining the individual Stokes parameters. In Fig. 2, we quantify how this inherent uncertainty affects our ability to measure the polarization state of backscattered light and ultimately, the polarizing properties of a sample.

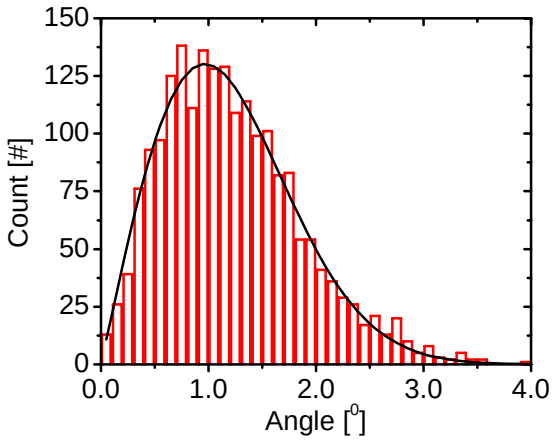

Fig. 2. Distribution of absolute values of angles between each of the 2048 Stokes vectors shown in Fig. 1 (left) and the mean Stokes vector, for each of the two incident polarization states. The solid black line shows a theoretical probability density function (Eq. 1) based on a 2-dimensional Gaussian distribution, fit to the measured data.

For each of the two polarization states shown in Fig. 1 (left), the absolute values of the angles between the mean Stokes vector and all 1024 individual Stokes vectors were determined, and displayed as a histogram in Fig. 2. The data demonstrated a mean angular deviation of 1.22° from the mean Stokes vector, with a standard deviation of 0.64°. A theoretical probability density function of the form

$$P(\theta;\theta_0,\sigma)=\frac{2\pi\theta}{\sigma\sqrt{2\pi}}\exp-\left(\frac{(\theta-\theta_0)}{2\sigma^2}\right) \quad (1)$$

#7740 - $15.00 US
Received 7 June 2005; revised 13 July 2005; accepted 14 July 2005

(based on a two-dimensional Gaussian noise distribution) was fit to the experimental data, and found to be in good agreement; $P(\chi^2; N) > 0.24$. A recent paper [25] presented a theoretical expression relating the same error in Stokes vector location on the Poincaré sphere, to the system SNR.

When a fiber-optic probe is scanned, bend-induced birefringence produces a change in the polarization state of light, which can be visualized as a change in the Stokes vector on the surface of the Poincaré sphere. The amount of phase retardation incurred between orthogonal components of polarized light is described by the rotation angle of the corresponding Stokes vector, and a material's optic axis orientation is defined as the axis around which this vector rotation is made. In Fig. 3, we quantify the effect of sample arm motion on the Stokes vectors by displaying the intensity-weighted mean phase retardation angle incurred by our pair of incident states as a function of A-line pair number, while the probe is held stationary and during a linear or rotary scan. On the left, the phase retardation angle remains close to zero while the probe is stationary, in the center, the retardation increases at a rate of 0.019 °/A-line pair with the linear scanning probe, while on the right, the phase retardation angle increases at a maximum rate of 1.64 °/A-line pair with the rotary probe. If we model the rotary probe as an arbitrary linear retarder with a rotating optic axis, the Stokes vector is expected to map out the same change in polarization state as the probe rotates from 0°-180° as from 180°-360°, and this appears to be the case in Figs. 1 and 3. Blue arrows in the center and right-hand graphs indicate the A-line range over which a single image frame is acquired, corresponding to 775 A-lines with each input polarization state for the linear probe, and 655 A-line pairs for the rotary probe.

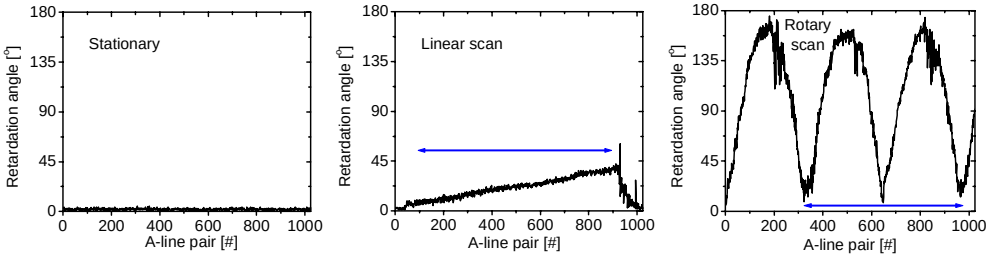

Fig. 3. Retardation angle (defined as the mean angle through which the Stokes vectors are rotated), for the pair of incident polarization states displayed in Fig. 1 left (stationary probe), center (linear scanning probe), and right (rotary scanning probe). Blue arrows indicate the scan range used to generate a single image.

To ensure that both our conventional and polarization-sensitive OCT images are not perturbed by motion-induced effects in the sample arm probe, we analyze interference fringe data using the Stokes vector formalism, with measurement of the polarization state of light at the sample surface for each A-line. Polarization-sensitive images are obtained by displaying the intensity-weighted mean phase retardation angle for our pair of incident states, relative to the polarization state of light at each location across the sample surface [18].

3.2 Measurements on a calibrated wave plate

To establish the magnitude of measurement errors associated with using a scanning fiber optic probe, we performed a series of measurements on a quarter wave plate, with the linear scanning device. The achromatic wave plate comprised two cemented pieces of different birefringent crystals, designed to minimize the variation in birefringence with wavelength. The plastic outer sheath of the linear scanning fiber probe was placed in contact with the wave plate. Strong reflections from the front and rear surfaces of the wave plate are seen in a plot of backscattered intensity (black) shown in Fig. 4, with a third peak at a depth of 867 μm originating from the interface between the two materials. The accumulated double-pass phase

#7740 - $15.00 US Received 7 June 2005; revised 13 July 2005; accepted 14 July 2005

retardation relative to the sample surface is shown in red, with Stokes parameters averaged over 64 A-lines and 5 points in depth. This curve begins at 0° at the sample surface, reaches around 85° at the cemented interface, and 174° at the lower surface of the wave plate.

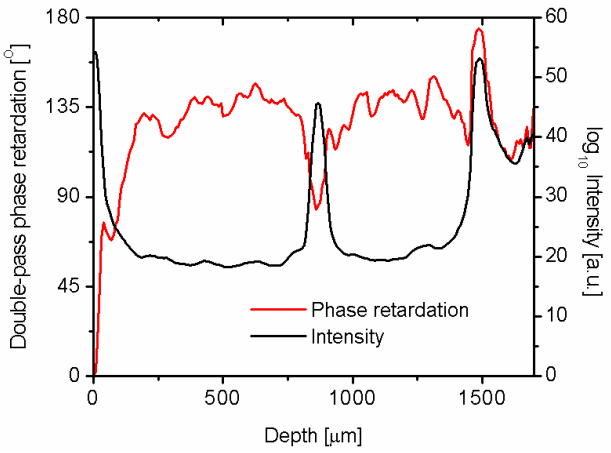

Fig. 4. Measured backscattered intensity and accumulated double-pass phase retardation for a quarter wave plate.

One would expect to obtain a phase retardation value of 180° for a λ/4 plate on double pass. However, an exact half-wave is the most difficult amount of retardance to measure, since due to wrap-around of the Stokes vector in the Poincaré sphere, values above 180° are never realized, and an actual retardation angle of $(180 + \theta)°$ will yield the value $(180 - \theta)°$. Averaging repeated measurements therefore produces a mean that does not converge on the expected value of 180°, but instead approaches some lower value. Table 1 presents measured double-pass phase retardation (DPPR) values, averaged over $n = 10$ successive B-scans, first with the probe held stationary, then scanning linearly in directions perpendicular and at 45° to the fast axis of the λ/4 plate.

Table 1. Measured values of double pass phase retardation (DPPR) for a quarter wave plate

	Mean DPPR (n = 10) [°]	Standard deviation [°]
No scanning	174.56	0.35
Scanning, 45° to fast axis	173.14	0.29
Scanning, ⊥ to fast axis	172.85	0.53

The results of Fig. 1 demonstrated that when the fiber probe is not scanned, the measured Stokes vectors exhibit a mean fluctuation of 1.22° on the Poincaré sphere during acquisition of the B-scan. When measuring the wave plate without scanning, a discrepancy is observed between the measured value of 174.56° and the expected value of 180°, which cannot be due to polarization effects associated with sample arm motion. This error amounts to around 3%, and is in agreement with an independent transmission measurement of the wave plate retardance, made using a Berek compensator. Deviation from exactly one-quarter wave retardance for spectral components different from the wave plate's design wavelength is also expected to result in measured DPPR values different from 180°. DPPR values obtained when the probe was scanning exhibit slightly higher errors of up to 4%, with this increase representing the magnitude of error attributable to motion-induced effects.

#7740 - $15.00 US
Received 7 June 2005; revised 13 July 2005; accepted 14 July 2005

3.3 Measurements on biological tissue

In Figs. 1 and 3, we presented the polarization states of light measured at the detectors, arising from reflections at the surface of the GRIN lens or prism at the distal tip of each probe. The previous sections used reflections from these optical-quality surfaces to isolate and quantify the effects of fiber motion on the polarization state of light in the system. However, when performing PS-OCT measurements in biological tissue, the incident polarization states must be obtained from reflections at the tissue surface due to the limited depth scanning range, resulting in an increased degree of uncertainty in determining the corresponding Stokes vectors. This uncertainty was previously reduced by using a pair of average surface Stokes vectors formed from all, or some range of A-lines in an image [18, 20]. A measure of the accuracy of this pair of average surface states is given by the offset from zero degrees of phase retardation calculated between the surface and first data point within the tissue. This analysis is carried out with the understanding that the tissue itself may contribute to the retardation offset, due to birefringence at the surface. For the sample shown in Fig. 5, a retardation angle of 0.82° is expected, based on a spatial dimension of 2.9 μm per depth point and a measured double-pass phase retardation rate of 0.28 °/μm.

In Fig. 5, the phase retardation offset is plotted as a function of the number of A-lines over which the Stokes vectors are averaged, for the tissue specimen imaged with the rotary probe, to be shown later in Fig. 7. Averaging is also performed over 3 and 6 points in depth for each case, where the term "points in depth" refers to the number of displayed data points in each A-line. As the number of averaged A-lines increases, the phase retardation offset is initially reduced, due to improved determination of the Stokes vectors. However, due to the fact that the surface states are continuously changing while the probe is scanning, averaging the Stokes vectors over increased numbers of A-lines does not reduce the offset beyond some limiting value.

It is worth noting that OCT imaging techniques with a sufficiently large depth scan range, such as optical frequency-domain imaging (OFDI), could use the reflections from optical components at the probe tip as surface states, and still maintain a useful imaging depth in the sample. However, this requires that any intermediate elements, including the sheath, do not introduce any change in the polarization state of light at the sample.

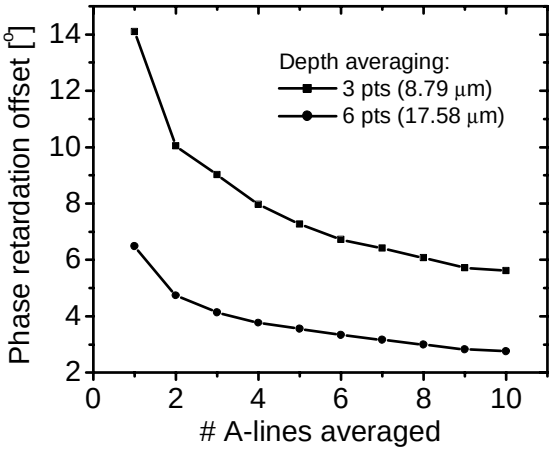

Fig. 5. Phase retardation angle measured between the surface and first point in depth within the tissue sample, as a function of the number of A-lines over which Stokes vectors are averaged, for the rotary probe example shown in Fig. 7.

PS-OCT images obtained with the scanning fiber probes are presented in Figs. 6 and 7. Conventional images of backscattered light intensity are displayed on a logarithmic gray scale, with black representing strongly backscattering regions. In the polarization-sensitive

#7740 - $15.00 US Received 7 June 2005; revised 13 July 2005; accepted 14 July 2005

images, we display the measured phase retardation angle between components of light resolved along the optic axes of the tissue, evolving from 0° (black) at the tissue surface, to 180° (white) to 360° (black). Before applying our polarization-sensitive algorithm [24], we averaged all measured polarization states by applying a finite-impulse-response filter to each of the Stokes parameters in the image, using two-dimensional correlation. The filter size was 4 A-lines by 6 points in depth, corresponding to averaging the backscattered polarization states over an area of 20.6 μm x 28.2 μm for the linear scanning probe, and 2.82° x 17.6 μm for the rotary probe.

One potential application of endoscopic PS-OCT is in orthopedics, where minimally-invasive procedures involving ligaments, tendons, cartilage and other birefringent tissues are commonplace. Figure 6 presents OCT images from a meniscal tissue sample, obtained under a protocol approved by the Institutional Review Board of Massachusetts General Hospital, from a patient undergoing knee replacement surgery.

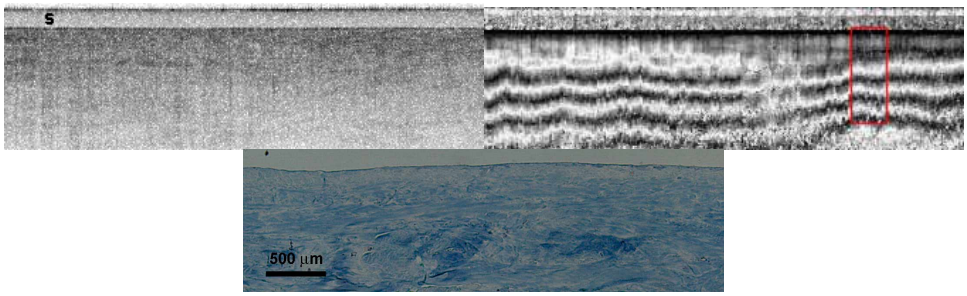

Fig. 6. Top: conventional (left) and polarization-sensitive (right) images of an *ex vivo* human meniscus specimen. The box indicates the region where the double-pass phase retardation rate is quantified (see text). Images are 4 mm wide and 1.2 mm deep. The probe sheath is indicated in the conventional OCT image (s). Bottom: corresponding histology with trichrome stain.

The medial and lateral meniscii are a pair of C-shaped pieces of fibrocartilage located at the peripheral aspect of the knee, providing stability, lubrication and shock absorption in the joint. As with articular cartilage, the meniscii are susceptible to damage and degeneration with age, requiring diagnosis and intervention to repair. In Fig. 6 (top left), with the probe sheath (s) placed in light contact with the tissue, the conventional OCT image from this meniscus specimen demonstrates a fairly homogeneous appearance. In the polarization-sensitive image (top right), the specimen appears strongly birefringent, with the polarization state of light seen to evolve rapidly on propagation in the tissue, as indicated by the multiple black-white bands. Although the frequency of these bands is seen to vary with location in the image, indicating variable levels of birefringence, a mean double-pass phase retardation rate of 1.33 ± 0.04 °/μm was measured within the region indicated. The corresponding histology (bottom) demonstrates the high density of collagen fibers in the meniscus, stained blue by the trichrome stain.

Another potential application of endoscopic PS-OCT is in cardiovascular imaging, where identification of vulnerable plaques and understanding the processes leading to their development is of considerable interest [1]. Figure 7 shows conventional and PS-OCT images from an *ex-vivo* coronary specimen, acquired using the rotary scanning probe. The main layers of the vessel wall are evident in the conventional OCT image (Fig. 7(a)). Moving outwards from the vessel lumen, the intima (i), media (m) and adventitia (a) are labeled [1], with each known to contain collagen in varying amounts with location [26]. The importance of referencing the polarization state of light backscattered from within the sample to individual states at the sample surface is illustrated by the corresponding polarization-sensitive images (b, c). Individual surface states were used in (b), and a single pair of averaged surface states was used in (c). The Stokes vectors representing these surface states

#7740 - $15.00 US Received 7 June 2005; revised 13 July 2005; accepted 14 July 2005

are shown in the Poincaré sphere (f), with the blue and green traces describing the continuously-changing surface states used in Fig. 7(b), and the red circles indicating the averaged states used in Fig. 7(c).

The use of averaged surface states is inappropriate in endoscopic PS-OCT and can lead to artifacts in the polarization-sensitive image. As can be seen in Fig. 7(c), retardation values at the sample surface appear as grayscale levels offset from 0° (black), corresponding to values significantly higher than expected based on the quantitative results shown in Fig. 5. Throughout the image, phase retardation values are incorrect in those A-lines where a non-zero angle exists between the average surface state and the true surface state.

The correct use of individual surface states (Fig. 7(b)) enables measurement of changes in the polarization state of backscattered light within the vessel wall, as the image pixels change from black at the inner surface, towards white, then to black again. The fact that phase retardation values of 180° (white) are not reached could be due to a change in collagen fiber orientation with depth in the sample. From the data displayed in Fig. 7(b), a mean double-pass phase retardation rate of 0.28 ± 0.005 °/μm was measured for this specimen. The corresponding H&E stained histology (d) shows the layers of the vessel wall, with collagen-rich tissue appearing blue in the trichrome stained section (e).

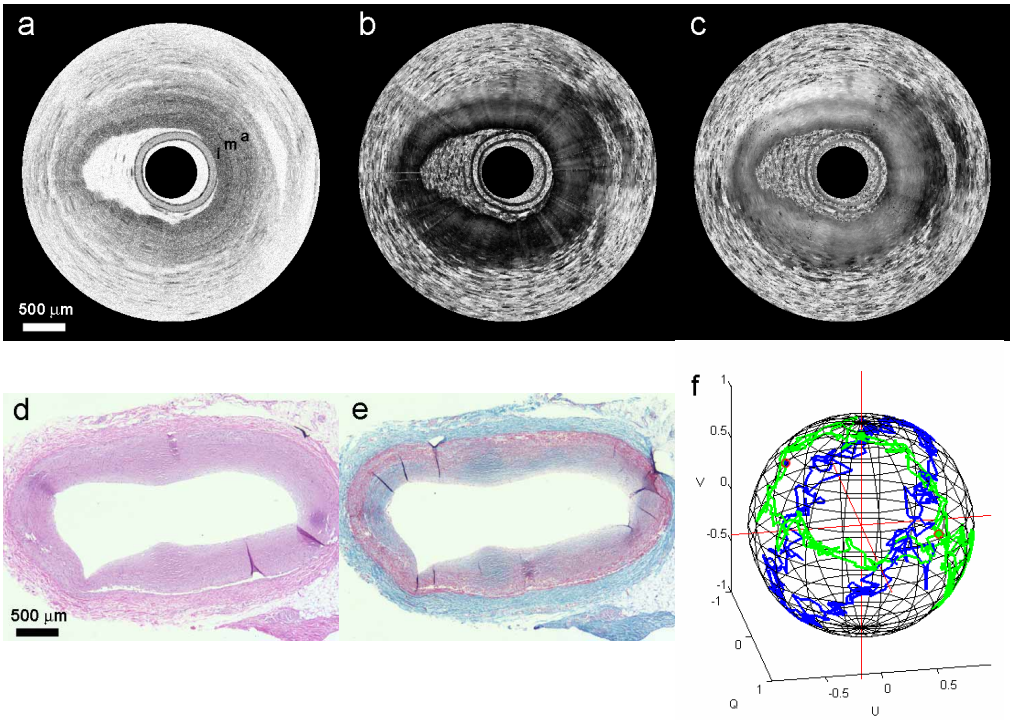

Fig. 7. Conventional (a) and polarization-sensitive (b, c) images of *ex-vivo* human coronary tissue, obtained with the rotary scanning probe. The polarization-sensitive images were generated using either individual surface states (b), or averaged surface states (c). Corresponding histologic sections, with H&E (d) and trichrome stain (e). Surface polarization states used to generate the polarization-sensitive images above (f). Scale bars = 0.5 mm.

4. Summary

Fiber-optic implementation has enabled OCT systems to be used in a wide range of clinical studies, including endoscopic procedures, where the technology represents a unique imaging tool for many internal organ systems. Polarization-sensitive OCT has also been demonstrated

#7740 - $15.00 US
Received 7 June 2005; revised 13 July 2005; accepted 14 July 2005

as an extension to conventional OCT, providing functional information by determining the polarization properties of tissues. To date, fiber-based PS-OCT systems have typically been used in the laboratory with a stationary sample arm and transverse scanning at the distal end, or in the clinic with only minimal fiber motion during acquisition of each A-line [27-29]. When a length of the sample arm fiber is actively translated or rotated in order to achieve transverse scanning (as is typically the case for endoscopic and catheter-based imaging), extraction of polarization-sensitive information becomes more challenging due to dynamic changes in fiber birefringence.

Our method reduces the influence of dynamic fiber birefringence by making a relative measurement, comparing the detected polarization state of light backscattered from within the sample, to the detected state from the tissue surface [18]. Sampling the incident polarization state for every A-line isolates motion-induced polarization artifacts to changes occurring on this timescale. Previously, surface states were calculated by averaging individual surface states across all, or some number of A-lines within an image. Using an average surface state reduces the error in determining the initial Stokes vector, with a corresponding improvement in determination of sample retardation and optic axis orientation. This averaging method is valid when the incident state is not changing, which is a reasonable assumption for most reported fiber-based PS-OCT systems. However, the evolution of incident states demonstrated in Fig. 1 indicates that this averaging technique should be limited to only a small number of neighboring A-lines when a scanning sample arm fiber is used. When only a few A-lines are utilized, we have demonstrated that high-quality PS-OCT image data may be obtained from scanning fiber probes in human tissue. While the specific form of the trace of the incident Stokes vectors on the Poincaré sphere will vary under different conditions and from one probe to another, the concepts for isolating motion-induced effects as presented in this manuscript remain applicable to polarization-sensitive imaging with any scanning fiber probe. This also applies to high-speed endoscopic imaging with spectral-domain PS-OCT systems, where an increase in sample arm scan speed will be accompanied by a proportional increase in the frequency of surface state sampling. In as much as most reported endoscopic OCT probes are based on the designs used here, we expect the principles laid out in this paper may be applied without loss of validity for accurate PS-OCT imaging with other endoscopic OCT systems.

This understanding and implementation of our PS-OCT algorithm in endoscopic imaging enhances the already growing application space for OCT. In otolaryngologic and orthopedic applications, the linear-scanning probe can be combined with standard endoscopic procedures to evaluate the location and integrity of collagen-rich tissues. Incorporation of polarization-sensitivity with the rotary probe will enable the collagen content of intravascular tissues to be investigated.

Acknowledgments

Funding from the National Institutes of Health (R01-RR-19768, R01-EY 14975), Department of Defense (F4 9620-01-10014) and the Center for Integration of Medicine and Innovative Technology (CIMIT) is gratefully acknowledged.